Proceedings of the ASME 2018 37th International Conference on Ocean, Offshore and Arctic Engineering
OMAE2018
June 17-22, 2018, Madrid, Spain

OMAE2018-77964

DRAFT: PIPELINE FRACTURE DUE TO COMPRESSION-TENSION LOADING CAUSED BY FOREIGN OBJECT IMPACT

Martin Kristoffersen*
Tore Børvik
Structural Impact Laboratory (SIMLab)
Centre for Advanced Structural Analysis (CASA)
Norwegian University of Science and Technology
Rich. Birkelands vei 1, NO-7491 Trondheim, Norway
E-mail: martin.kristoffersen@ntnu.no

Lars Olovsson

IMPETUS Afea AB
Sördalavägen 22,
SE-14160 Huddinge, Sweden
E-mail: lars@impetus.no

ABSTRACT

In areas frequented by fishing vessels, trawl equipment or anchors may interfere with pipelines and cause damage through impact, potential hooking, and ensuing release of the pipeline. This load sequence of denting followed by global bending and springback results in a complex stress and strain history. Experiments have shown that fracture in an impacted pipe typically arises along the bottom of the dent, where the material suffers high compressive strains in the impact and hooking phase, and a rapid change to tension during the rebound phase. High compressive strains may reduce the strain to failure significantly for a succeeding tensile phase. A common trait of ductile damage models is to account for damage through nucleation, growth and coalescence of voids, which traditionally is thought to occur during tension. In this study, an uncoupled phenomenological Cockcroft-Latham-type fracture model accounting for anisotropic damage is used. The fracture model is implemented in the explicit finite element programme IMPETUS Afea Solver, and calibrated using material tests. Simulations show that the proposed fracture model is able to account for the observed behaviour.

INTRODUCTION

Today and for all foreseeable future, steel pipelines are and will be used extensively for transporting oil and gas. These pipelines are situated in potentially dangerous environments, where impact loads from foreign objects like anchors or trawl gear pose a particularly hazardous threat [1]. Pipe impact tests have shown that fracture is likely to occur directly underneath the striker during the elastic recovery after maximum displacement [2, 3]. In this area of the pipe the material is heavily compressed before the loading is reversed into tension, a load sequence that can cause a ductile-to-brittle transition [4]. Earlier, Ludley and Drucker [5] made bent-beam specimens which emulate the strain history from the pipe (compression followed by tension), and a ductile-to-brittle transition was observed at room temperature for an estimated 60% precompressive engineering strain. A similar approach was adopted by Manes et al. [6], who used strips of an X65 offshore pipeline steel.

Several studies have considered material behaviour subsequent to a prescribed prestrain. Drucker et al. [7] compressed cylindrical specimens in the range of 10% to at most 45% engineering strain, where the specimens were machined to their original shape for approximately each 3% strain increment to ensure as uniform compression as possible. Subsequent tensile tests showed a reduced strain to failure with increasing compression, a shift to more brittle fracture surfaces, and even a shear fracture mode for the highest compression level. Fukuda et al. [8] demonstrated that both compressive and tensile prestrain reduced the critical crack tip opening displacement for various offshore steels, where compressive strains had a larger effect than tensile. Bouchard et al. [9] investigated the effect of

*Corresponding author

particle distribution on reverse loading of ductile steels, while Bao and Wierzbicki [10] used notched and cylindrical specimens for compression testing of a 2024-T351 aluminium alloy, in which fracture initiated by shear in the equatorial area. For the same alloy, combined tension/compression/torsion experiments on tubular specimens were carried out by Papasidero et al. [11]. Their experimental results indicated that precompression can increase the ductility of aluminium 2024-T351. Notched X65 steel specimens compressed to large values of true strain before being stretched to failure in tension showed a reduced tensile strain to failure [4], and a transition to shear fracture for the highest compression levels. Compression-tension tests (up to 13% engineering strain) on DP780 dual phase steel sheets using an anti-buckling device suggested that the strain to fracture increased with increasing compression [12]. In summary, the strain path has been shown to be of significant importance [13–15].

This study aims to use a new phenomenological Cockcroft-Latham [16] (CL) type fracture model to account for the fracture observed when stretching X65 pipelines bent after impact [17]. The new fracture criterion has been implemented in the explicit finite element programme IMPETUS Afea Solver. Material data from the literature is used for the X65 material, and applied to simulations of the full load cycle of impact and subsequent stretching of a pipeline. The numerical results are generally in good agreement with the experimental data, and shows a proof of concept for the new fracture model.

MATERIAL TESTING

Description of the X65 steel

The material in the pipes used in this study is an X65 grade steel, a material widely used in pipelines conveying oil and/or gas. According to the material inspection certificate, the yield strength is 450 MPa and the ultimate tensile strength is 535 MPa. Young's modulus is 208 000 MPa. Previous work has shown that for engineering purposes, the material is homogeneous and isotropic [4]. The pipes used are made seamless by utilising the Mannesmann effect, and are supplied by Tenaris, Argentina.

Tension tests

Quasi-static material tests are carried out on smooth and notched axisymmetric specimens (notch root radius $R = 0.8$ mm and 2.0 mm), shown in Fig. 1(a). By using a micrometer precision laser on a mobile frame [17], the minimum diameter of the specimens was measured continuously throughout each test. This allows calculation of the true stress and true strain up to fracture (average values over the cross-section), and this has been plotted in Fig. 1(b). Based on 12 smooth specimens, the yield stress (and standard deviation) was found as 478 ± 15 MPa, the ultimate tensile strength 572 ± 14 MPa, and the true fracture strain $\varepsilon_f = 1.61 \pm 0.03$ as measured by [18]

$$\varepsilon_f = \ln\left(\frac{A_0}{A_f}\right) \tag{1}$$

where A_0 is the initial cross-sectional area of the specimen, and A_f the area at fracture, obtained by meausing the diameter using a micrometer measurement tool. The fracture surfaces were circular, thus indicating an isotropic material. The stress triaxiality σ^* is defined as the ratio between the hydrostatic stress σ_H and the equivalent stress σ_{eq}, and this ratio increases with a sharper notch. From Fig. 1 it is noted that a sharper notch, and

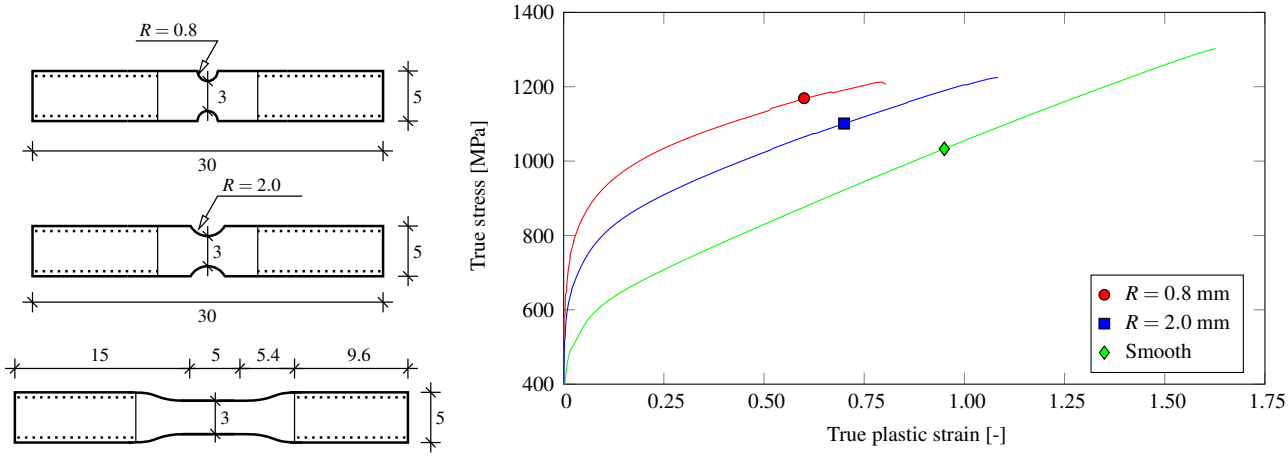

(a) Specimen geometries

(b) Tensile test results

FIGURE 1. Tenstile tests, where (a) shows the axisymmetric specimen geometry and (b) representative true stress-true plastic strain curves.

hence higher σ^*, leads to a reduction in fracture strain – which was meaured to 1.08 ± 0.05 for $R = 2.0$ mm and 0.77 ± 0.02 for $R = 0.8$ mm. Dynamic tension tests on the smooth specimens showed a moderate strain rate sensitivity, with about 20% increase of the flow stress at a strain rate of 830 s^{-1}. The fracture strain, however, appeared unaffected by the strain rate [3].

Compression-tension tests

Compression tension tests have been carried out to see how the level of precompression affects the following tensile phase [4]. Notched, axisymmetric specimens (shown in Fig. 2) have been compressed to a prescribed level of true strain before being stretched to failure in tension. Five true strain compression levels were attained – 0, 0.10, 0.20, 0.30 and 0.40.

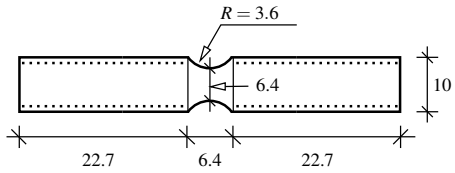

FIGURE 2. Notched specimen for compression-tension loading.

All five true stress-true plastic strain curves are plotted in Fig. 3. At load reversal, each specimen has a compressed cross-sectional area A_r, which is used to calculate a relative strain to failure ε_r

$$\varepsilon_r = \ln\left(\frac{A_r}{A_f}\right) \tag{2}$$

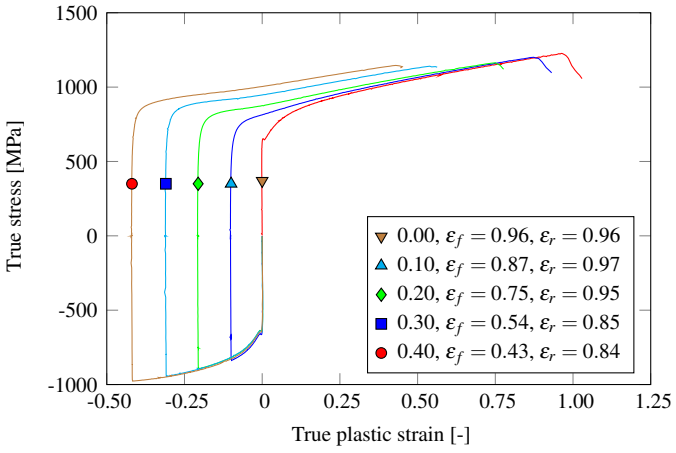

FIGURE 3. True stress-true plastic strain curves from compression-tension tests on notched specimens.

As seen, this value decreases when the strain in the compressive phase exceeds 0.20 (see Fig. 3). A different specimen geometry allowing compressive strains up to 1.00 has shown that ε_r decreases even further with increasing compression and with increasing magnitude of negative stress triaxiality [19].

The absolute fracture strain as in Eqn. (1) decreases even more than the relative fracture strain. From a value of 0.96 for pure tension, ε_f decreases to 0.87, 0.75, 0.54, and 0.43 for compression strains of 0.10, 0.20, 0.30 and 0.40, respectively. This may increase the probability of fracture in a pipe impact scenario, where the material is compressed and then stretched in the dent (discussed in more detail in Refs. [4, 19]). The new fracture criterion proposed herein attempts to account for the effect of this compression-tension loading sequence.

MATERIAL MODELLING

Constitutive relation

The Johnson-Cook (JC) constitutive relation [20] accounts for isotropic hardening, strain rate sensitivity and temperature softening, and is used with the von Mises yield criterion and the associated flow rule. The von Mises equivalent stress is a function of the deviatoric part of the Cauchy stress tensor $\boldsymbol{\sigma}$,

$$\sigma_{\text{eq}}(\boldsymbol{\sigma}) = \sqrt{\frac{3}{2}\boldsymbol{\sigma}^{\text{dev}} : \boldsymbol{\sigma}^{\text{dev}}} \tag{3}$$

The JC flow stress σ_{JC} is expressed by

$$\sigma_{\text{JC}}\left(\varepsilon_{\text{eq}}, \dot{\varepsilon}^*_{\text{eq}}, T^*\right) = \left(A + B\varepsilon^n_{\text{eq}}\right)\left(1 + C\ln\dot{\varepsilon}^*_{\text{eq}}\right)\left(1 - T^{*m}\right) \tag{4}$$

in which A, B, n, C and m are material constants, and ε_{eq} is the equivalent plastic strain. The dimensionless plastic strain rate is given by $\dot{\varepsilon}^*_{\text{eq}} = \dot{\varepsilon}_{\text{eq}}/\dot{\varepsilon}_0$, where $\dot{\varepsilon}_0$ is a user-defined reference strain rate defining the limit for quasi-static conditions, and $\dot{\varepsilon}_{\text{eq}}$ is the equivalent plastic strain rate. The homologous temperature is defined as $T^* = (T - T_r)/(T_m - T_r)$, where T is the absolute temperature, T_r is the ambient temperature and T_m is the melting temperature of the material. The problem herein is assumed to be isothermal, thus omitting the temperature bracket of Eqn. (4),

$$\sigma_{\text{JC}}\left(\varepsilon_{\text{eq}}, \dot{\varepsilon}_{\text{eq}}\right) = \left(A + B\varepsilon^n_{\text{eq}}\right)\left(1 + C\cdot\ln\frac{\dot{\varepsilon}_{\text{eq}}}{\dot{\varepsilon}_0}\right) \tag{5}$$

Then, from Eqn. (3) and Eqn. (5), the dynamic yield function f_{JC} becomes

$$f_{\text{JC}}\left(\boldsymbol{\sigma}, \varepsilon_{\text{eq}}, \dot{\varepsilon}_{\text{eq}}\right) = \sigma_{\text{eq}}(\boldsymbol{\sigma}) - \sigma_{\text{JC}}\left(\varepsilon_{\text{eq}}, \dot{\varepsilon}_{\text{eq}}\right) \tag{6}$$

where $f_{\text{JC}} \leq 0$ implies elastic behaviour, while $f_{\text{JC}} > 0$ indicates viscoplastic behaviour. The initial size of the yield surface is given by the constant A.

Fracture model

Many fracture criteria used in numerical simulations are based on damage through void growth in tension. The fracture criterion suggested by Cockcroft and Latham [16] is based on what may be visualised as a kind of "plastic work". In simple terms, this phenomenological criterion states that damage grows during plastic straining as long as the major principal stress σ_1 is positive (tension), meaning that compression is not accounted for. When the "plastic work" by $\sigma_1 > 0$ reaches a certain critical value W_{cr}, failure occurs. W_{cr} is obtained from the area under the true stress-true strain curve from a smooth uniaxial tensile test (see Fig. 1(b)). It is expressed quite simply in mathematical terms as

$$D = \frac{1}{W_{\text{cr}}} \cdot \int_0^{\varepsilon_{\text{eq}}} \langle \sigma_1 \rangle \, \mathrm{d}\varepsilon_{\text{eq}} \tag{7}$$

where D is the damage parameter, which upon reaching unity signifies failure. The Macauley bracket notation used in Eqn. (7) has the following definition,

$$\langle \sigma_1 \rangle = \begin{cases} \sigma_1 & \text{if } \sigma_1 \geq 0 \\ 0 & \text{if } \sigma_1 < 0 \end{cases} \tag{8}$$

The newly proposed fracture model implemented in IMPETUS Afea Solver has the same form as Eqn. (7), in which σ_1 is replaced by the largest eigenvalue $\hat{\sigma}_1$ of an augmented stress tensor $\hat{\boldsymbol{\sigma}}$,

$$\hat{\boldsymbol{\sigma}} = \mathbf{A}\boldsymbol{\sigma}\mathbf{A}^{\text{T}} \tag{9}$$

where $\mathbf{A}$ is a real symmetric tensor describing the effect of compression. $\mathbf{A}$ is a function of the principal stretches $\lambda_1 \geq \lambda_2 \geq \lambda_3$, and their adhering eigenvectors $\mathbf{v}_1$, $\mathbf{v}_2$ and $\mathbf{v}_3$,

$$\mathbf{A} = \sum_{i=1}^{3} \left(\frac{\lambda_1}{\lambda_i} \right)^{\eta} \mathbf{v}_i \otimes \mathbf{v}_i \tag{10}$$

Here, η is a new dimensionless scalar parameter, where $\eta = 0$ reduces the new model to the original CL criterion. Also, in proportional loading where λ_1 coincides with σ_1, the new model behaves like the CL criterion.

Calibration and validation

The material constants for the constitutive relation in Eqn. (5) was taken from the literature [21], where the calibration was based on quasi-static and dynamic uniaxial tension tests on the smooth geometry in Fig. 1(a). The value $W_{\text{cr}} = 1562$ MPa (average of 12 tests) for the new fracture model was obtained by integration of true stress-true plastic strain curve for the smooth specimen in Fig. 1. Finally, $\eta = 0.8$ was found through inverse modelling of the compression-tension tests.

Simulations of the material tests from Fig. 1 were run as validation cases using IMPETUS Afea Solver. Quarter symmetry was used in the numerical models as the material is isotropic, and fully integrated 64-node cubic elements were used to mesh the specimens with an element size of approximately 0.5 mm. To keep the simulation time at a reasonable level, a time scaling factor of 10^{-3} was applied and the strain rate sensitivity parameter in the material model was set to zero. The energy balance was typically of the order of 3% kinetic energy or less for these simulations, which is acceptable. When the damage parameter D attains unity in one of the 64 Gauss points in each element, the material fails by a node-splitting algorithm [22]. The exterior node closest to the integration point is split, and new element faces are created so that the crack plane is orthogonal to the maximum principal stress.

The results are shown in Fig. 4. As in the experiments, the curves are average values over the minimum cross-section. The strain ε over the current area A is $\varepsilon = \ln(A/A_0)$ and the stress is $\sigma = F/A$ in which F is the reaction force on the specimen shoulder in the axial direction. During testing the stress and strain distribution is not necessarily homogeneous across the minimum

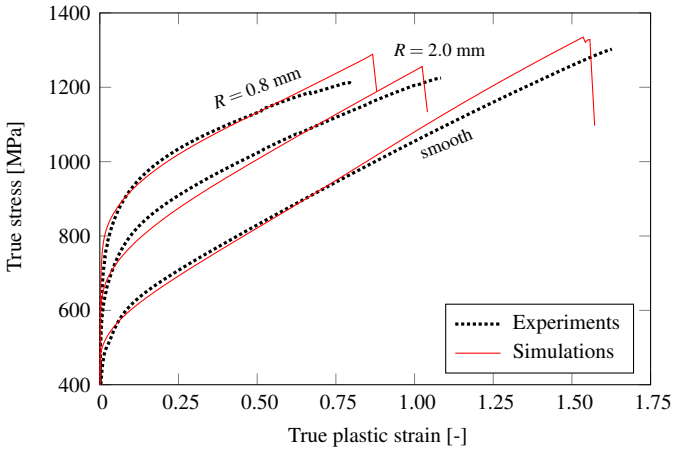

FIGURE 4. Simulations of tensile tests with $\eta = 0.8$.

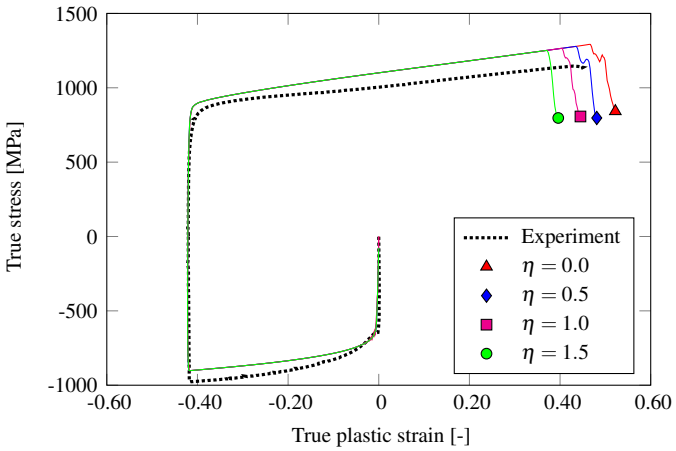

FIGURE 5. Simulations illustrating the effect of η on the tensile strain to failure of compression to a true strain 0.40.

cross-section, making this an approximation.

As seen in Fig. 4, the fit is quite good but deviates somewhat for large strain values (above 0.8). A more detailed material model may ameliorate this effect. The calibration of the JC model is as mentioned based on the smooth specimen only, so the behaviour is well predicted for the notched geometries. For $R = 0.8$ mm the failure strain is overpredicted, and for the other two geometries it is underpredicted.

A simulation of precompression to 0.40 true strain before tension tension loading to failure was run to illustrate the effect of η. When $\eta = 0$ the new criterion behaves like the original CL criterion. Increasing the value of η results in a decrease of the tensile strain to failure after compression as shown in Fig. 5, and the effect is larger for larger compressive strains. For this case, the chosen value of $\eta = 0.8$ gives an absolute fracture strain of 0.42. For comparison, the experimental value is 0.43.

Regarding the stress-strain behaviour, it is observed that the stress is somewhat underpredicted in the inital compression phase. A similar trend is observed for strains below 0.50 in the tension tests from Fig. 4. As the model only includes isotropic hardening, the yield stress after load reversal is overpredicted. In addition the experiments show signs of work hardening stagnation, which is not captured by the numerical model used herein. A natural extension of the current work would be to include the effect of kinematic hardening.

COMPONENT TESTS

Experimental setup

The component tests are designed to emulate the impact, bending and subsequent stretching of a pipe caused by trawl gear or anchor impact. Fig. 6 illustrates a real case compared with the somehwat simplified experimental setup used in previ-

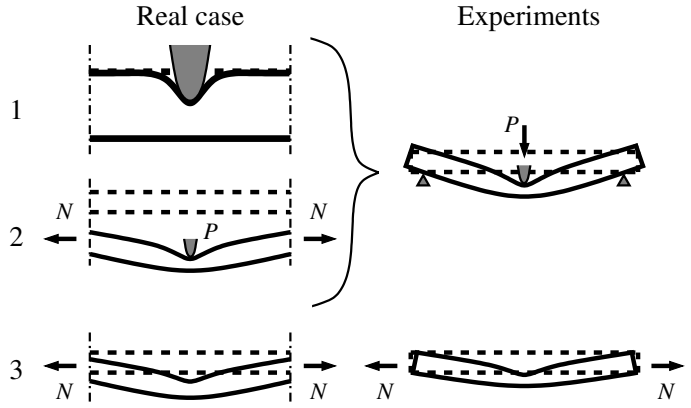

FIGURE 6. Comparison of reality and experiments, respectively the left and right part of the figure. The dotted lines indicate the initial position of the pipe, while the solid lines signify the displacements. Stage 1 (labels on the left) is zoomed in for clarity, and the sketch is not to scale [4].

ous work [4]. When a real pipeline is impacted and deflected by a force P from a foreign object, an axial force N arises in the pipeline [23], making it recoil towards its initial position when P is removed. The main physics of this load cycle is recreated in the experiments by a three-point bending dynamic impact load followed by a quasi-static stretch phase.

For the impact phase, a trolley with mass 1472 kg is accelerated to a certain velocity before it strikes a simply supported pipe. While the impact location can be of significance [24], this study is limited to impact at midspan. The nose of the trolley has the sharpest nose radius ($r = 10$ mm) specified in the DNV-GL recommended practice [1]. A load cell behind the indenter on the trolley registers the force.

Two impact velocities are presented herein, $v_A = 3.24$ m/s and $v_B = 5.13$ m/s, for pipe A and pipe B respectively. These velocities are in the upper end of what can be expected by fishing trawlers. The pipes have an internal diameter of 123 mm, and a wall thickness of $t_p \approx 4$ mm (varies slightly between each pipe). At the cylindrical supports with diameter $D_s = 50$ mm,

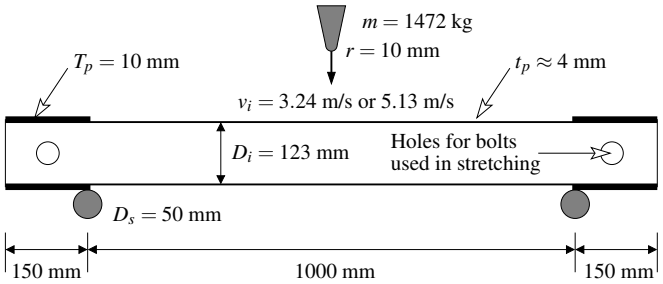

FIGURE 7. Schematic sketch of the dynamic impact test.

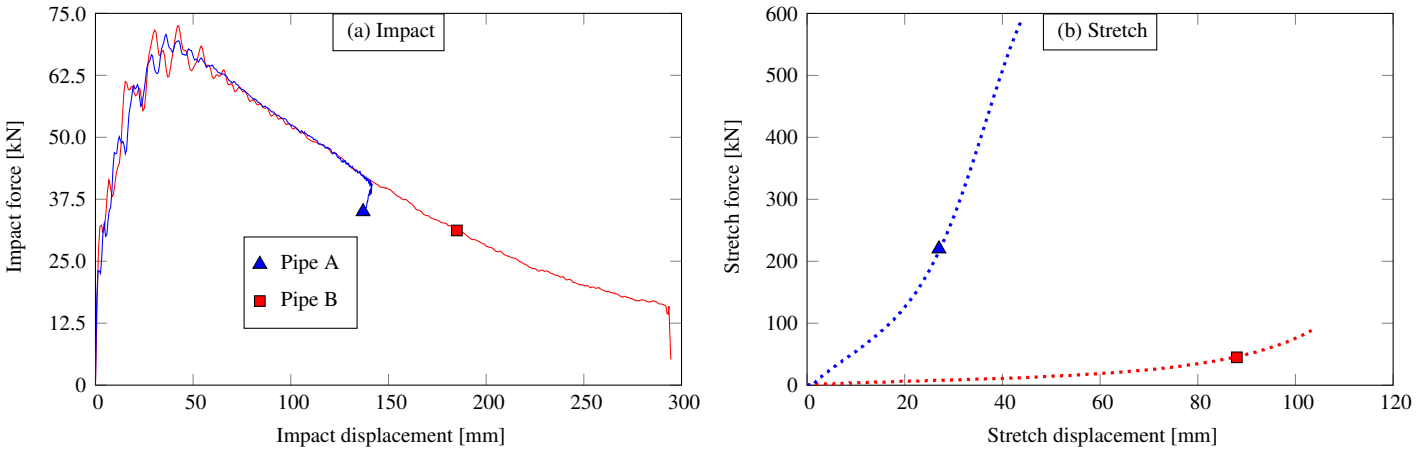

FIGURE 8. Force-displacement curves from the component tests, where (a) shows the data from the impact part and (b) data from the stretch part.

the pipe wall thickness T_p is 10 mm. Fig. 7 shows a sketch of the three-point bending impact test setup, Table 1 lists various details related to the tests. After impact, the deformed pipes are straightened quasi-statically at a deformation rate of 20 mm/min in a universal testing rig

Test results

Fig. 8 shows force-displacement curves from both the impact phase (solid lines) and the stretch phase (dotted lines). A low-pass filter has been applied to the impact curves to remove the high frequency noise from the recordings. As observed, the curves are similar in shape and magnitude in the impact phase. Pipe A absorbs all the kinetic energy of the trolley travelling at $v_A = 3.24$ m/s, and attains a maximum transverse displacement of about 140 mm. A sketch of a deformed pipe after impact is shown in Fig. 9, with adhereing values in Table 1. Note that w_i includes the rotation of the pipe ends, and is therefore not equal to the impact displacement in Fig. 8(a). For the higher velocity (pipe B, $v_B = 5.13$ m/s) the pipe deforms more to absorb the higher kinetic energy. Nevertheless, the trolley hits the buffers in the rig, thus limiting the maximum deformation of the pipe to about 300 mm. The amplitude of the local oscillations appear to be somehwat smaller for the lower velocity, and the period of the oscillations is roughly equal to the period of the second eigenmode.

The stretch phase (part (b) in Fig. 8) is completely different manners for pipe A and B. Pipe A, with the least transverse deformation, is straightened fairly quickly and is able to resist the applied load by a tensile force through the length of the pipe. Pipe B, however, is much more deformed and has to withstand a sizeable bending moment before the force can be resisted by tension. In addition, only surface cracks were observed for pipe A, while pipe B suffered through-thickness cracks (see Ref. [4] for

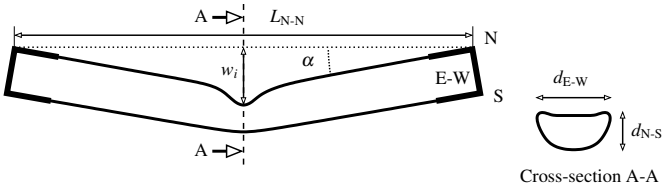

FIGURE 9. Typical outline of deformation shape (not to scale) of pipes after impact testing only, along with explanation of measurements given in Table 1.

details). The force level at which a surface crack was observed by visual inspection in the stretch phase was about 100 kN for pipe A, and below 20 kN for pipe B. It is likely that Pipe B was cracked immediately after impact due to the springback, as other experiments have shown that this happens for velocities of this magnitude [3]. This necessarily reduces the load bearing capacity of the pipe during stretching by a significant amount.

NUMERICAL SIMULATIONS

Simulations have been run using the explicit finite element code IMPETUS Afea Solver, featuring GPU implementation and acceleration. The numerical setup is in essense a recreation of the experimental setup sketched in Fig. 7, and the mesh used for the simulations is shown in Fig. 10.

Numerical setup

One plane of symmetry along the main pipe axis has been utilised, and both supports have been modelled as hollow rigid cylinders with diameter $D_s = 50$ mm. All degrees of freedom are fixed for the supports. The indenter is also represented by a rigid part, and is given the desired initial velocity and an appropriate density making the total mass 736 kg due to the symmetry plane.

TABLE 1. Experimental and numerical data ($\eta = 0.8$) from pipe impact tests. See Fig. 9 for explanation of measurements.

Pipe		**Exp. A**	**Num. A**	**Exp. B**	**Num. B**
Trolley mass	[kg]	1472	1472	1472	1472
Nose radius	[mm]	10	10	10	10
Avg. thickness	[mm]	3.89±0.36	3.85	3.86±0.34	3.85
Initial velocity	[m/s]	3.24	3.24	5.13	5.13
Kinetic energy	[J]	7708	7727	19356	19371
Peak impact force	[kN]	70.7	70.0	72.7	72.6
w_i	[mm]	170	167	333	329
$L_{\text{N-N}}$	[mm]	1250	1244	1104	1103
$d_{\text{N-S}}$	[mm]	60	60	22	24
$d_{\text{E-W}}$	[mm]	180	179	199	198
α	[deg]	12	10	30	25

Futher, the indenter displacement during the impact phase is limited by a fixed plate representing the buffers in the experiments. Contact between the different parts is ensured by the penalty approach. The pipe wall thickness was set to 3.85 mm for both A and B, although this measure varies slightly (see Table 1).

The impact phase is over when contact between the pipe and the indenter has ceased after maximum displacement. After impact, the residual velocities in the pipe are removed and a damping load is applied to reduce the residual stresses. The bolts used for stretching are added when the stretch phase commences, and are modelled as rigid, hollow cylinders. The stretch phase is applied by pinning one of the bolts running through the pipe, and applying a smoothly ramped displacement to the other bolt.

All parts are meshed by fully integrated 64-node cubic solid elements, giving an accurate representation of the curved surfaces in this problem. The element size in the pipe is decreased underneath the indenter as this region will be most deformed.

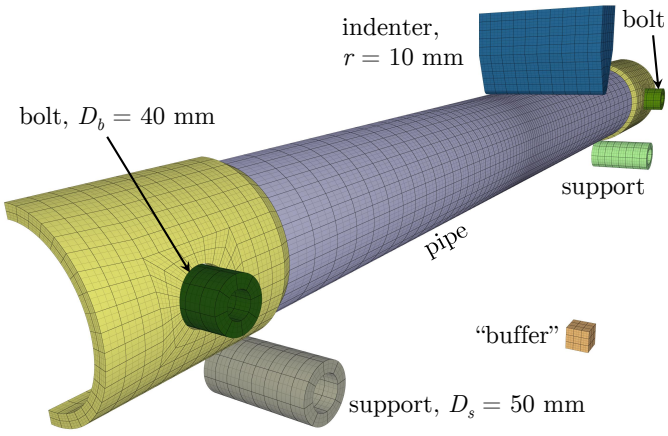

FIGURE 10. Mesh used in simulations of the component tests. The thick lines indicate the element boundaries.

In this area, the element length in the axial direction is about 4.5 mm, and in the circumferential direction it is 8.0 mm. The entire pipe has two elements across the thickness, and seven nodes across the thickness on account of the cubic elements. This might be a bit coarse to capture the nuances of crack initiation and propagation, but the global behaviour should be accurately represented. The X65 material is modelled by the JC model [20] and the new uncoupled damage model with node-splitting as described above.

Simulation results

The experiments are generally well represented by the simulations, for both pipe A and pipe B (see Table 1). Fig. 11 shows the force-displacement curves of both the impact phase (a) and the stretch phase (b) of pipe A, while Fig. 12 contains the same data for pipe B. As seen, the impact phase matches the experiments well in both cases, in terms of initial stiffness, peak load, and maximum displacement. The numerical results have been filtered like the experimental results. During the impact phase, the simulation results have somewhat higher amplitude oscillations than the experiments, particularly for pipe A. Besides the filtering, this could indicate that the material inhibits some damping properties which are not included in the simulations, or that rigid supports with fixed nodes affects the behaviour. The general force level is still well represented by the simulations. These measurements have been shown to be sensitive to the pipe wall thickness used in the simulation [25].

For pipe B the experimental deformation is limited by buffers – included in the simulations as an elastic stop plate beyond which the indenter can not pass (enforced by penalty based contact). This approach works well in limiting the deformation of pipe B like in the experiments. After the impact phase is over, the damage parameter D was 0.24 for pipe A with $\eta = 0.0$, and 0.27 for $\eta = 0.8$. For pipe B, D was 0.37 for $\eta = 0.0$ and 0.40

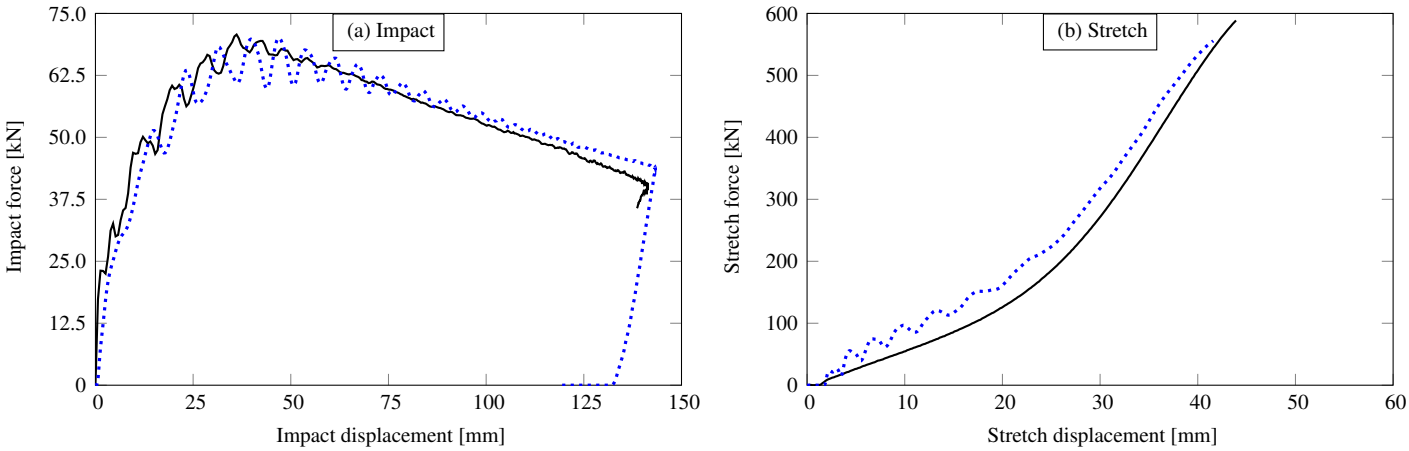

FIGURE 11. Force-displacement curves from experiments (solid curves) and simulations (dotted curves) of pipe A, where (a) shows the impact data and (b) the stretch data. For these simulations, there were no differences between using $\eta = 0.0$ and $\eta = 0.8$.

for $\eta = 0.8$. Using different values of η does not affect the force-displacement curves in the impact phase.

The force level is overpredicted in the beginning of the stretch phase for both cases, and some residual oscillations from the impact can be seen. No fracture occured for pipe A for both values of η. While the inclination of the curve looks fairly good for pipe A, it is overpredicted for pipe B. The strain rates in the impact simulations are typically of the order of 10^2 s^{-1} for both pipes, and the difference in strain rate between the pipes is very small. Fig. 12(b) shows that the stretch phase for pipe B starts out the same for both values of η, but diverges when the first fracture occurs for $\eta = 0.8$ (near the markers on the curves). After this, each new elment face created due to node splitting causes a sudden change in the stiffness and hence a notable slant in the force-displacement curve. In the experiments, crack growth is not a discrete event but a continuous process which a coarse discretisation is unable to represent satisfactorily. A finer discretisation could ameliorate this, and provide a more even crack growth. Still, the new fracture criterion is able to account for an earlier onset of fracture due to compression-tension loading, exampli-fied by both the material and component test simulations. While the pipe did not crack directly after impact as observed in experiments [3], it did during stretching – which is an improvement over previously obtained results [17]. The maximum compressive strain in the pipes' axial direction right after impact was 0.68 in pipe A and 0.96 in pipe B (for both values of η). A complete through-thickness crack appeared in the simulation, resembling the experimental data qualitatively (shown in Fig. 13). Quanti-

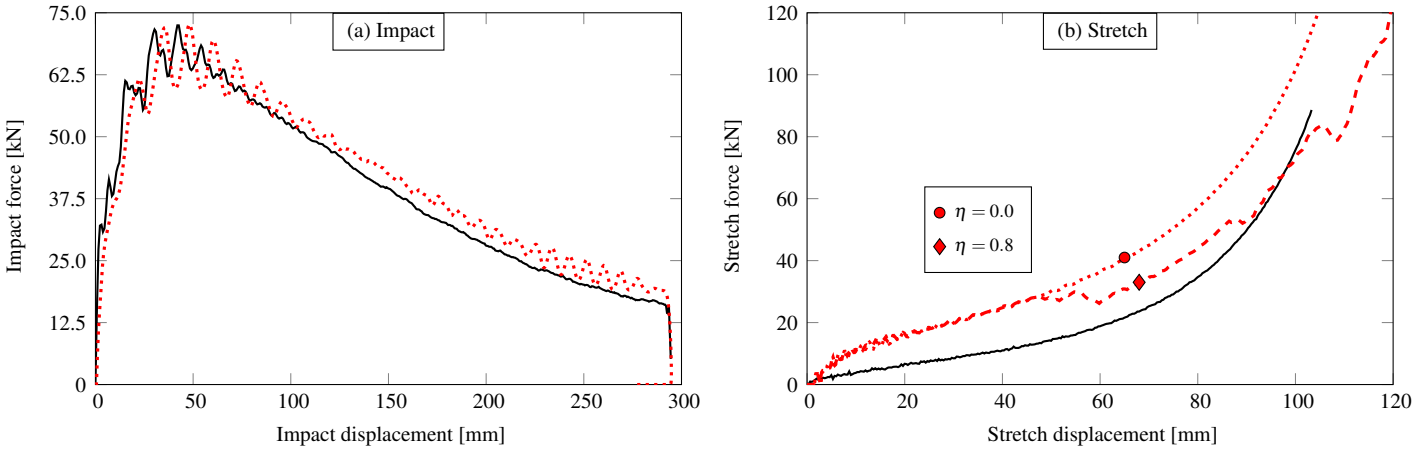

FIGURE 12. Force-displacement curves from experiments (solid curves) and simulations of pipe B (dotted curves) of (a) the impact phase, and (b) the stretch phase with two different values of η. The impact phase was unaffected by η.

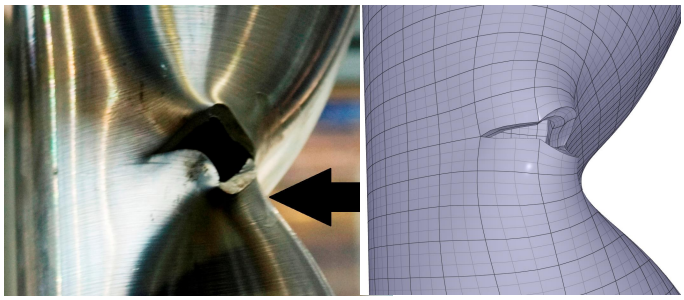

FIGURE 13. Comparison between experiment (left) and simulation (right) during stretching of pipe B.

tatively, the impact phase is well represented, as Table 1 attests to. The force in the stretch phase is however somewhat overpredicted, as fracture does not initiate directly after impact.

DISCUSSION AND CONCLUDING REMARKS

The compression-tension material tests show that the strain to failure decreases with increasing compression. By adding only one extra parameter η compared with the fairly simple CL criterion [16], a new phenomenological fracture model is proposed in an attempt to capture the effect of compression on the strain to failure in subsequent tension. Fig. 5 shows the effect of η, which accounts for the observed behaviour. Higher values of η reduces the strain to failure after compression. In general, the new fracture criterion is able to account for the reduction in tensile failure strain caused by a compressive load prior to the tensile phase, and a proof of concept has been established. The stress-strain behaviour is not ideally captured due to the material model, since only isotropic hardening is included. In addition, the stress level is somewhat overpredicted for large true strain values (above 0.8).

The impact phase of the component tests are well captured, as are the post-impact geometric measurements of the pipes. In the stretch phase, the results in terms of force-displacement curves are improved compared with previous results although the force is slightly overpredicted. The calibration of η was based on tests up to a precompression of 0.40 true strain, while in the impact tests the compressive strains were 0.68 for pipe A and 0.96 for pipe B. Provided an improved calibration is obtained, this approach is promising for future work – which should aim to account for kinematic hardening and include additional validation cases for the model. Further, only one pipe wall thickness was examined numerically. By expanding the parameter study to include this measure, better results could be obtained as the thickness has been shown to affect the pipe behaviour notably. For models like the ones used herein, mesh sensitivity can be an important issue and warrants further investigation.

ACKNOWLEDGMENT

The authors gratefully appreciate the financial support from NTNU and the Research Council of Norway through the Centre for Advanced Structural Analysis, Project No. 237885 (CASA). Statoil ASA has generously supplied the X65 steel pipes used in this study.

REFERENCES

[1] DNV GL AS, 2014. *Offshore standard DNV-RP-F111: Interference between trawl gear and pipelines*. Det Norske Veritas Germanischer Lloyd AS.

[2] Jones, N., and Birch, R., 1996. "Influence of internal pressure on the impact behaviour of steel pipelines". *International Journal of Pressure Vessel Technology,* ***118***, pp. 464–471.

[3] Kristoffersen, M., Børvik, T., Langseth, M., and Hopperstad, O., 2016. "Dynamic versus quasi-static loading of X65 steel pipes". *European Physical Journal – Special Topics,* ***225***, pp. 325–334.

[4] Kristoffersen, M., Børvik, T., Westermann, I., Langseth, M., and Hopperstad, O., 2013. "Impact against X65 steel pipes – An experimental investigation". *International Journal of Solids and Structures,* ***50***, pp. 3430–3445.

[5] Ludley, J., and Drucker, D., 1960. "A Reversed-Bend Test to Study Ductile to Brittle Transition". *Welding Journal (Research Supplements),* ***39***, pp. 543–546.

[6] Manes, A., Porcaro, R., Ilstad, H., Levold, E., Langseth, M., and Børvik, T., 2012. "The behaviour of an offshore steel pipeline material subjected to stretching and bending". *Ships and Offshore Structures,* ***7***, pp. 371–387.

[7] Drucker, D., Mylonas, C., and Lianis, G., 1960. "Exhaustion of Ductility of E-Steel in Tension Following Compressive Prestrain". *Welding Journal (Research Supplements),* ***39***, pp. 117–120.

[8] Fukuda, N., Hagiwara, N., and Masuda, T., 2005. "Effect of Prestrain on Tensile and Fracture Toughness Properties of Line Pipes". *Journal of Offshore Mechanics and Arctic Engineering,* ***127***, pp. 263–268.

[9] Bouchard, P., Bourgeon, L., Lachapele, H., Maire, E., Verdu, C., Forestier, R., and Loge, R., 2008. "On the influence of particle distribution and reverse loading on damage mechanisms of ductile steels". *Materials Science and Engineering A,* ***496***, pp. 223–233.

[10] Bao, Y., and Wierzbicki, T., 2004. "On fracture locus in the equivalent strain and stress triaxiality space". *International Journal of Mechanical Sciences,* ***46***, pp. 81–98.

[11] Papasidero, J., Doquet, V., and Mohr, D., 2015. "Ductile fracture of aluminum 2024-T351 under proportional and non-proportional multi-axial loading: Bao-Wierzbicki results revisited". *International Journal of Solids and Structures,* ***69-70***, pp. 459–474.

[12] Marcadet, S., and Mohr, D., 2015. "Effect of compression-tension loading reversal on the strain to fracture of dual phase steel sheets". *International Journal of Plasticity,* ***72***, pp. 21–43.

[13] Vaz Jr, M., de Santi Jr, N., and de Souza Neto, E., 2010. "Numerical Prediction of Ductile Failure Onset under Tensile and Compressive Stress States". *International Journal of Damage Mechanics,* ***19***, pp. 175–195.

[14] Benzerga, A., Surovik, D., and Keralavarma, S., 2012. "On the path-dependence of the fracture locus in ductile materials – Analysis". *International Journal of Plasticity,* ***37***, pp. 157–170.

[15] Dæhli, L., Børvik, T., and Hopperstad, O., 2016. "Influence of loading path on ductile fracture of tensile specimens made from aluminium alloys". *International Journal of Solids and Structures,* ***88***, pp. 17–34.

[16] Cockcroft, M., and Latham, D., 1968. "Ductility and the workability of metals". *Journal of the Institute of Metals,* ***96***, pp. 33–39.

[17] Kristoffersen, M., Børvik, T., Langseth, M., Ilstad, H., Levold, E., and Hopperstad, O., 2013. "Damage and failure in an X65 steel pipeline caused by trawl gear impact". *Proceedings of the ASME 2013 32nd International Conference on Ocean, Offshore and Arctic Engineering, Nantes, France*. Paper no. 11277.

[18] Liu, B., Villavicencio, R., and Soares, C., 2015. "Shear and tensile failure of thin aluminium plates struck by cylindrical and spherical indenters". *Ships and Offshore Structures,* ***10***, pp. 45–58.

[19] Kristoffersen, M., Børvik, T., and Hopperstad, O., 2016. "Using unit cell simulations to investigate fracture due to compression-tension loading". *Engineering Fracture Mechanics,* ***162***, pp. 269–289.

[20] Johnson, G., and Cook, W., 1983. "A constitutive model and data for metals subjected to large strains, high strain rates and high temperatures". *Proceedings of the* 7^{th} *International Symposium on Ballistics*, pp. 541–547.

[21] Kristoffersen, M., Casadei, F., Børvik, T., Langseth, M., and Hopperstad, O., 2014. "Impact against empty and water-filled X65 steel pipes – Experiments and simulations". *International Journal of Impact Engineering,* ***71***, pp. 73–88.

[22] Olovsson, L., Limido, J., Lacome, J.-L., Hanssen, A., and Petit, J., 2015. "Modling fragmentation with new high order finite element technology and node splitting". *European Physical Journal – Web of Conferences,* ***94***.

[23] Kristoffersen, M., Langseth, M., and Børvik, T., 2017. "Combined three-point bending and axial tension of pressurised and unpressurised X65 offshore steel pipes – Experiments and simulations". *Submitted for possible journal publication*.

[24] Liu, B., and Soares, C., 2017. "Influence of impact location on the plastic response and failure of rectangular cross section tubes struc transversely by a hemispherical indenter". *Journal of Offshore Mechanics and Arctic Engineering,* ***139***.

[25] Kristoffersen, M., Casadei, F., Børvik, T., Langseth, M., Solomos, G., and Hopperstad, O., 2013. "Numerical simulations of submerged and pressurised X65 steel pipes". *XII International Conference on Computational Plasticity, Barcelona, Spain*.